Global model of a magnetized ion thruster with xenon and iodine

IEPC-2019-678

R. Lucken,[*] F. Marmuse [†], A. Bourdon,[‡] P. Chabert[§]

Laboratoire de Physique des Plasmas, CNRS, Sorbonne Université,
UPMC Universités Paris 6, Université Paris Sud, Université Paris Saclay,
École polytechnique, F-91128 Palaiseau Cedex, France

and

A. Tavant [¶]

Safran Aircaft Engines, Vernon, France, and
Laboratoire de Physique des Plasmas, CNRS, Sorbonne Université,
UPMC Universités Paris 6, Université Paris Sud, Université Paris Saclay,
École polytechnique, F-91128 Palaiseau Cedex, France

Gridded ion thrusters are proven technologies for spacecraft propulsion in the Earth environment and beyond for commercial, scientific and exploratory missions. Experimental works and theoretical investigations have shown that the efficiency of these thrusters can be improved by magnetic confinement. However, it is known that instabilities develop in magnetized plasmas that deconfine the electrons and decrease the efficiency with respect to what the classical theory of stable plasma transport predicts. Using recent theories of instability enhanced plasma transport, and based on former works performed on the global modeling of plasma discharges in the non-magnetized case, we develop a global model of a gridded ion thruster where the plasma is sustained by a radio-frequency antenna, and confined by a magnetic field oriented along the thrust axis. The unstable xenon plasma is simulated using 2D PIC simulation in simplified geometry. Iodine and xenon thrusters are both simulated using the global model, with a magnetic field varying between 0 and 20 mT. The plasma properties predicted by the classical and the instability enhanced transport models are given. The performances of the thrusters are also compared.

[*]Ph.D. student, Université Paris Saclay, romain.lucken@lpp.polytechnique.fr.
[†]Ph.D. student, Université Paris Saclay, florian.marmuse@lpp.polytechnique.fr.
[‡]Research director, Centre National de la Recherche Scientifique, anne.bourdon@lpp.polytechnique.fr.
[§]Research director, Centre National de la Recherche Scientifique, pascal.chabert@lpp.polytechnique.fr
[¶]Ph. D. student, antoine.tavant@lpp.polytechnique.fr

Nomenclature

n	=	Species densities, m^{-3}
T	=	Species temperatures, K (or eV when specified)
m	=	Particle mass, kg and ion masses
R	=	Thruster radius, m
L	=	Thruster length, m
β_g	=	Grid transparency
β_i	=	Ion transparency
S_g	=	Outlet surface for the gas
S_i	=	Outlet surface for the ions
S	=	Total thruster inner surface (grid holes included)
V	=	Thruster volume
ϕ_s	=	Sheath potential, V
Q	=	Gas flow rate, sccm (part./m^3)
$\mathcal{P}_{RF}$	=	RF power, W
$\mathcal{P}_{plume}$	=	Plume power, W
P_{abs}	=	Absorbed power, W/m^3
ζ	=	Power coupling efficiency
B	=	Magnetic field, T
k_B	=	Boltzmann constant, J/K
γ_s	=	Wall recombination coefficient
$\overline{v}$	=	Thermal speed, m/s
u_B	=	Bohm speed, m/s
κ	=	Rate of surface power loss (normalized to $k_B T_e$)
K_{el}	=	Electron-neutral elastic collision rate factor, m^3/s
ν_e	=	Electron-neutral momentum transfer collision frequency, s^{-1}
ν_{eff}	=	Effective electron-neutral momentum transfer collision frequency, s^{-1}
$K_{ex,j}, \mathcal{E}_{ex,j}$	=	Electron-neutral excitation reaction rate factor j, and energy threshold, m^3/s and J
$K_{iz}, \mathcal{E}_{iz}$	=	Electron impact ionization rate factor and ionization energy, m^3/s and J
$K_{diss}, \mathcal{E}_{diss}$	=	Electron impact dissociation rate factor and dissociation energy, m^3/s and J
$K_{dissiz}, \mathcal{E}_{dissiz}$	=	Electron impact dissociative ionization rate factor and energy, m^3/s and J
K_{dissat}	=	Electron impact dissociative attachment rate, m^3/s
K_{dissat}	=	Ion-ion recombination rate, m^3/s
λ_i	=	Ion mean free path, m
$\mathbf{\Gamma}_i$	=	Ion flux, part./(m^2 s)
h_L	=	Longitudinal ion loss coefficient
h_R	=	Radial ion loss coefficient
$h_{R,0}$	=	Radial ion loss coefficient at $B = 0$
$h_{R,0}$	=	Radial ion loss coefficient at large B
h	=	Global ion losses coefficient
G	=	Ratio betwen the $h_{R,B}$ and $h_{R,0}$
P_{abs}	=	Power absorbed by the plasma, W/m^3
P_{loss}	=	Power lost in the discharge volume and at the boundaries, W/m^3
γ	=	Thrust power efficiency
η	=	Mass utilization efficiency

CPU	= computational power unit
GIT	= gridded ion thruster
ICP	= inductively coupled plasma
LEO	= low earth orbit
MCC	= Monte Carlo collision
PIC	= particle-in-cell
RF	= radio-frequency

I.   Introduction

Global models of gridded ion thrusters (GIT) can be of great help to optimize performance and design. These models are based on balance equations for the main characteristics of the plasma, such as species densities and temperatures. These models were successfully implemented to describe non-magnetized thruster discharges, but only few attempts were made to provide accurate modeling of GIT with a magnetic field.[1] However, several experimental studies have shown that the performances of GIT were considerably enhanced when an external magic field is applied.[12] In this paper, we propose a global model of a cylindrical GIT as depicted in Figure 1. In this thruster, the radio-frequency (RF) heating antenna is wired around the discharge chamber. A magnetic circuit produces a permanent axial magnetic field, along the thrust axis. In the modeling of such a thruster, two main difficulties arise:

1. The power coupling in presence of a magnetic field involves wave heating that is more difficult to predict than in the non magnetized case where the induced heating electric field inside the plasma is purely azimuthal and can be estimated through the scalar plasma permittivity. This issue was addressed in previous previous publications. The power coupling efficiency can be maximized by choosing an RF frequency near the electron cyclotron frequency. The coupling between the plasma and the heating antenna may also lead to strongly inhomogeneous plasma distributions that may limit the validity of 0D models.

2. Besides an enhanced power coupling efficiency, the magnetic field also improves the plasma confinement perpendicularly to the magnetic field lines, i.e., in the radial direction. Better plasma confinement leads to a lower electron temperature and a higher plasma density for the same power absorbed by the plasma, and same gas pressure. The classical magnetized plasma transport models fail to describe the time-averaged discharge equilibrium because large amplitude instabilities tend to develop in magnetized plasmas. This issue has not been very much investigated in the past in the context of GIT studies. Recent theoretical works based on PIC simulations can give hints about how the classical transport theory may be corrected.

In the first section, the general equations for global models of GITs operated with xenon and iodine are pro- vided. Next, 2D PIC simulation results in Cartesian coordinates are presented and the effect of instabilities on the magnetic confinement is discussed. The predicted plasma characteristics and thruster performances are then presented.

II.   Model Description

A.   General assumptions

The models presented below mainly come from Chabert et al.[4] for xenon and Grondein et al.[8] Considering the minor effect of the gas temperature in the most commmon regime where the gas temperature is much smaller than the electron temperature, the balance equations for the gas temperature was neglected. All the heavy species are assumed to be at the same temperature of $300\,\mathrm{K}$. The neutral gas is injected in the discharge chamber with a flow rate Q of typically a few sccm ($1\,\mathrm{sccm} = 4.49 \times 10^{17}\,\mathrm{particles\,/\,m^3}$) such that the gas pressure is usually between a fraction of mTorr and 10 mTorr. The electron temperature is essential to resolve the dynamic of the system as electron impact processes drive the ionization balance and the gas balance. The model is 0D such that all the plasma properties are assumed spatially uniform. Nevertheless, positive ion losses at the walls are accounted for by a factor labeled h that represents the ion flux at the walls normalized to the Bohm flux.
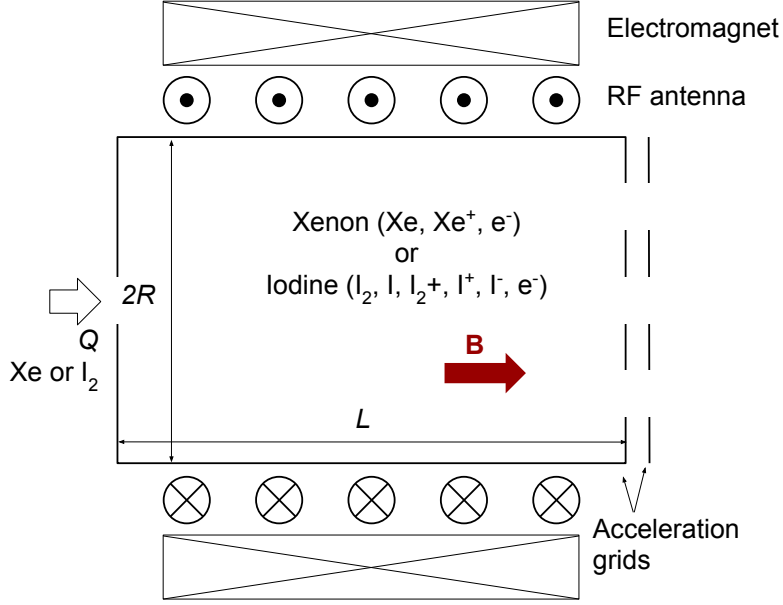
Figure 1. Schematic of the thruster simulated with the global models described in this paper.

$$h = \frac{\oiint_S \boldsymbol{\Gamma}_i \cdot \mathbf{dS}}{S n_i u_{B,i}} \tag{1}$$

where $\boldsymbol{\Gamma}_i$ is the flux, n_i is the density at the center, and

$$u_{B,i} = \left(\frac{k_B T_e}{m_i} \right)^{1/2} \tag{2}$$

is the Bohm speed of the positive ion species indexed by i. In Eq. (1), S stands for the surface area of the inner walls of the reactor. The h factor is also known as the edge-to-center density ratios for 1D discharges. In cylindrical geometries, it is useful to introduce

$$h_L = \frac{\oiint_{z=\pm L/2} \boldsymbol{\Gamma}_i \cdot \mathbf{dS}}{2\pi R^2 n_i u_{B,i}} \quad \text{and} \tag{3}$$

$$h_R = \frac{\oiint_{r=R} \boldsymbol{\Gamma}_i \cdot \mathrm{dS}}{2\pi R L n_i u_{B,i}} \tag{4}$$

to separate the pre-sheath drops in the axial and radial directions, respectively. The surface defined by $z = \pm L/2$ represents the top and bottom sides of the cylindrical thruster, and the surface defined by $r = R$ represents the cylindrical side surface. The total surface is the reunion of these two surfaces. Therefore,

$$h = \frac{(R h_L + L h_R)}{R + L} \tag{5}$$

At low to intermediate gas pressures, the wall losses are very important to determine both the electron temperature and the density of the various species. The expressions used for h_L and h_R will be given and discussed in paragraph D.

In the following, excited atoms are not tracked in the model, and excitation reactions are accounted for in the electron energy balance equation exclusively, using averages over several physical excitation levels.

B. Xenon model

The modeling of the electron-neutral reactions in the xenon thruster is based on the reaction set selected by V. Croes from the Biagi database on LXCat.[2] It accounts for elastic scattering, electron impact ionization, and four level-averaged excitation reactions as presented in Table 1.

The species included in the model are only Xe, Xe^+ and the electrons (e^-). However, assuming that the plasma sheaths near the reactor walls are small, the plasma can be seen as quasineutral, such that

$$n_{Xe^+} = n_{e^-} . \tag{6}$$

Reaction		Process	Rate [m³/s]	Threshold [eV]
$Xe + e^- \longrightarrow$	$Xe + e^-$	Elastic	K_{el}	0
$Xe + e^- \longrightarrow$	$Xe + 2e^-$	Ionization	K_{iz}	8.315
$Xe + e^- \longrightarrow$	$Xe^* + e^-$	Excitation 1	$K_{ex,1}$	9.447
$Xe + e^- \longrightarrow$	$Xe^* + e^-$	Excitation 2	$K_{ex,2}$	9.917
$Xe + e^- \longrightarrow$	$Xe^* + e^-$	Excitation 3	$K_{ex,3}$	11.7
$Xe + e^- \longrightarrow$	$Xe^* + e^-$	Excitation 4	$K_{ex,4}$	12.13

Table 1. Electron-neutral collision model used in the xenon PIC simulations and global model. The cross sections were extracted from the program Magboltz, version 7.1 June 2004[2]

The system of equations to be solved is hence

$$\frac{dn_{Xe^+}}{dt} = K_{iz}n_{Xe}n_{Xe^+} - hn_{Xe^+}u_{B,Xe^+}\frac{S}{V} \tag{7}$$

$$\frac{dn_{Xe}}{dt} = \frac{Q}{V} + n_{Xe^+}u_{B,Xe^+}\frac{hS - h_L S_i}{V} - K_{iz}n_{Xe}n_{Xe^+} - \frac{1}{4}n_{Xe}\overline{v}_{Xe} \tag{8}$$

$$\frac{d}{dt}\left(\frac{3}{2}n_{Xe}k_B T_e\right) = P_{abs} - P_{loss} \tag{9}$$

The system is almost identical to the paper by Chabert et al,[4] with slightly different notations and no gas temperature equation. The neutral flux of particles leaving the discharge chamber on the right-hand-side (RHS) of Eq. (8) is a thermal flux with a thermal velocity

$$\overline{v}_{Xe} = \left(\frac{8k_B T_g}{\pi m_{Xe}}\right)^{1/2} = 220\text{m/s at } T_g = 300\text{K} \tag{10}$$

In Eq. (9), P_{abs} is the power density absorbed by the plasma, which is an input of the model (we do not consider the power coupling efficiency to the RF generator here), and P_{loss} is the power density lost by the electrons through volume reactions and surface losses.

In the case of the xenon model,

$$P_{\text{loss}} = \gamma_i \mathcal{E}_{iz} K_{iz} + 3\frac{m_e}{m_{Xe}}k_B(T_e - T_g)K_{el}n_{Xe^+}n_{Xe} + \kappa k_B T_e h u_{B,Xe^+}n_{Xe^+} \tag{11}$$

$$= \left(E_{iz}K_{iz} + \sum_{j=1}^{N_{ex}}E_{ex,j}K_{ex,j} + 3\frac{m_e}{m_i}k(T_e - T_g)K_{el}\right)Vn_g\tilde{n}N + \kappa kT_e hSu_B N \tag{12}$$

The factor $\kappa k_B T_e$ represents the energy lost per electron leaving the plasma towards the walls and

$$\mathcal{E}_{iz}\gamma_i = \mathcal{E}_{iz} + \sum_{j=1}^{4}\mathcal{E}_{ex,j}K_{ex,j}/K_{iz} \tag{13}$$

is the mean energy lost in inelastic processes per electron-ion pair created. According to Chabert:[5]

$$\kappa = 2 + \frac{1}{2}\ln\left(\frac{m_i}{2\pi m_e}\right) \tag{14}$$

For xenon, $\kappa \approx 7.3$.

C.   Iodine model

The iodine model from the paper by Grondein et al.[8] is based on the same principles as the xenon model. The species considered in the model are I, I_2, I_2^+, I^+, I and the electrons. The list of reactions considered is provided in Table 2. Compared to the previous paper,[8] electron impact detachment from the I^- ion, electron impact dissociation of I_2^+ and non-resonant charge exchange reaction between I^+ and I_2 were added.

Reaction		Process	Rate m^3/s	Threshold [eV]	Reference
Electron impact I					
$I + e^- \longrightarrow$	$I + e^-$	Elastic	$K_{el,I}$	0	9
$I + e^- \longrightarrow$	$I + 2e^-$	Ionization	$K_{iz,I}$	11.64	9
$I + e^- \longrightarrow$	$I^* + e^-$	Excitation	$K_{ex,I}$	0.9529	9
Electron impact I_2					
$I_2 + e^- \longrightarrow$	$I_2 + e^-$	Elastic	K_{el,I_2}	0	9
$I_2 + e^- \longrightarrow$	$I_2^+ + 2e^-$	Ionization	K_{iz,I_2}	9.31	9
$I_2 + e^- \longrightarrow$	$I^+ + I + 2e^-$	Dissociative ionization	K_{dissiz}	10.75	9
$I_2 + e^- \longrightarrow$	$I^- + I$	Dissociative attachment	K_{dissat}	0	9
$I_2 + e^- \longrightarrow$	$2I + e^-$	Dissociation	K_{diss,I_2}	1.567	9
Electron impact dissociation of I_2^+					
$I_2^+ + e^- \longrightarrow$	$I^+ + I + e^-$	Dissociation	K_{diss,I_2^+}	2.17	10
Electron detachment from I^-					
$I^- + e^- \longrightarrow$	$I + 2e^-$	Detachment	K_{det}	2.1768	10
Recombination					
$I^- + I_2^+ \longrightarrow$	$I + I_2$	Mutual neutralization	K_{rec,I_2^+}	0	7
$I^- + I^+ \longrightarrow$	$2I$	Mutual neutralization	K_{rec,I^+}	0	21
$I_2 + I^+ \longrightarrow$	$I_2^+ + I$	Charge exchange	K_{cex}	0	18+11
Surface recombination					
$I \longrightarrow$	$\frac{1}{2}I_2$	Wall process	γ_s (no unit)	0	6

Table 2. List of the reactions used in the iodine global model

The reaction rates for I^- detachment were computed by Quantemol by the R-matrix method for a wide range of electron energies.[10,20] The non-resonant charge exchange reaction between I^+ and I_2 is a function of the gas temperature, which is fixed here. The particle balance equations for each species are

$$\frac{dn_e}{dt} = K_{iz,\text{I}} n_e n_\text{I} + K_{iz,\text{I}_2} n_e n_{\text{I}_2} + K_{dissiz} n_e n_{\text{I}_2} - K_{dissat} n_e n_{\text{I}_2} + K_{det} n_e n_{\text{I}^-} \tag{15}$$

$$- h \left(n_{\text{I}^+} u_{B,\text{I}^+} + n_{\text{I}_2^+} u_{B,\text{I}_2^+} \right) \frac{S}{V} \tag{16}$$

$$\frac{dn_{\text{I}^-}}{dt} = K_{dissat} n_e n_{\text{I}_2} - K_{rec,\text{I}_2^+} n_{\text{I}^-} n_{\text{I}_2^+} - K_{rec,\text{I}^+} n_{\text{I}^-} n_{\text{I}^+} - K_{det} n_e n_{\text{I}^-} \tag{17}$$

$$\frac{dn_{\text{I}_2}}{dt} = \frac{Q}{V} - \left(K_{dissat} + K_{dissiz} + K_{iz,\text{I}_2} + K_{diss,\text{I}_2} \right) n_{\text{I}_2} n_e + K_{rec,\text{I}_2^+} n_{\text{I}-n_\text{I}^+} - K_{cex} n_{\text{I}_2} n_{\text{I}^+} \tag{18}$$

$$+ \frac{\gamma_s}{2} \frac{1}{4} n_\text{I} \bar{v}_\text{I} \frac{(S - S_g)}{V} - \frac{1}{4} n_{\text{I}_2} \bar{v}_{\text{I}_2} \frac{S_g}{V} + n_{\text{I}_2^+} u_{B,\text{I}_2^+} \frac{(hS - h_L S_i)}{V} \tag{19}$$

$$\frac{dn_\text{I}}{dt} = \left(K_{dissiz} + K_{dissat} + 2K_{dissat} \right) n_e n_{\text{I}_2} + 2K_{rec,\text{I}^+} n_{\text{I}^+} n_{\text{I}^-} + K_{rec,\text{I}_2^+} n_{\text{I}^-} n_{\text{I}_2^+} - K_{iz,1} n_e n_\text{I} + K_{diss,\text{I}_2^+} n_e n_{\text{I}_2^+} \tag{20}$$

$$+ K_{det} n_e n_{\text{I}^-} + K_{cex} n_{\text{I}_2} n_{\text{I}^+} - \gamma_s \frac{1}{4} n_\text{I} \bar{v}_\text{I} \frac{(S - S_g)}{V} - \frac{1}{4} n_\text{I} \bar{v}_\text{I} \frac{S_g}{V} + n_{\text{I}^+} u_{B,\text{I}^+} \frac{(hS - h_L S_i)}{V} \tag{21}$$

$$\frac{dn_{\text{I}_2^+}}{dt} = K_{iz,\text{I}_2} n_{\text{I}_2} n_e - K_{rec,\text{I}_2^+} n_{\text{I}^-} n_{\text{I}_2^+} + K_{cex} n_{\text{I}_2} n_{\text{I}^+} - K_{diss,\text{I}_2^+} n_e n_{\text{I}_2^+} - h n_{\text{I}_2^+} u_{B,\text{I}_2^+} \frac{S}{V} \tag{22}$$

$$\frac{dn_{\text{I}^+}}{dt} = K_{iz,\text{I}} n_e n_\text{I} + K_{dissiz} n_e n_{\text{I}_2} - K_{rec,\text{I}^+} n_{\text{I}^-} n_{\text{I}^+} - K_{cex} n_{\text{I}_2} n_{\text{I}^+} - h n_{\text{I}^+} u_{B,\text{I}^+} \frac{S}{V} \tag{23}$$

The electron power balance equation has the same form as Eq. (9) but the absorbed power term needs to be slightly modified to account for the more complex chemistry of iodine. Similarly to xenon, electron energy issue lost by elastic collisions, excitation reactions and ionization with the neutral gas (I and I_2 in this case). But energy thresholds corresponding to dissociative ionization, I_2 and I_2^+ dissociation, and electron detachment from I also need to be subtracted. In summary,

$$P_{loss} = \left[\left(\mathcal{E}_{iz,1} K_{iz,1} + \mathcal{E}_{ex,1} K_{ex,\text{I}} \right) n_\text{I} + \left(\mathcal{E}_{iz,\text{I}_2} K_{iz,\text{I}_2} + \mathcal{E}_{dissiz} K_{dissiz} + \mathcal{E}_{diss,\text{I}_2} K_{diss,\text{I}_2} \right) n_{\text{I}_2} + \mathcal{E}_{det} K_{det} n_\text{I} \right. \tag{24}$$

$$\left. + \mathcal{E}_{diss,\text{I}_2^K} K_{diss,\text{I}_2^+} n_{\text{I}_2^+} + 3m_e \left(\frac{K_{el,\text{I}} n_\text{I}}{m_\text{I}} + \frac{K_{el,\text{I}_2} n_{\text{I}_2}}{m_{\text{I}_2}} \right) \right] n_e + \kappa k_B T_e \frac{hS}{V} \left(n_\text{I} + u_{B,\text{I}^+} + n_{\text{I}_2^+} u_{B,\text{I}_2^+} \right) \tag{25}$$

The κ coefficient represents the mean energy lost per electron leaving the discharge. According to Chabert[5]

$$\kappa = 2 + \frac{e\phi_s}{k_B T_e} \tag{26}$$

where ϕ_s is the sheath potential. The sheath potential can be calculated using the current balance between the positive ions that are accelerated through the sheath and the thermal flux of electrons. If we neglect the flux on negative ions that leave the plasma, and since $T_\text{I} \ll T_e$,

$$\kappa = 2 - \ln \left(\frac{\sqrt{2\pi m_e}}{n_{\text{I}^+} + n_{\text{I}_2^+}} \left[\frac{n_{\text{I}^+}}{m_\text{I}} + \frac{n_{\text{I}_2^+}}{m_{\text{I}_2}} \right] \right) \; . \tag{27}$$

On the contrary to the xenon discharge, the coefficient depends on the ion densities. It varies between 7.3 when only I^+ is present and 7.6 when only I_2^+ is present.

D. Plasma confinement

Since the magnetic field is along z, the transport in the z direction can be represented using the non-magnetized edge-to-center plasma density ratio[5]

$$h_L = 0.86 \left[3 + 0.5 \frac{L}{\lambda_i} + 0.2 \frac{T_i}{T_e} \left(\frac{L}{\lambda_i} \right)^2 \right]^{-0.5} \tag{28}$$

where λ_i is the ion mean free path. In the radial direction, the transport is limited by the magnetic field lines. This cylindrical configuration has been studied by Sternberg and Godyak[19] using classical theory in the low to intermediate pressure regimes. One of the main results was the following heuristic formula

$$h_R = h_{R,0} \left(1 + G + G^2\right)^{-1/2} \tag{29}$$

where $h_{R,0}$ is the 1D edge-to-center density ratio of a non-magnetized cylindrical discharge and

$$G = h_{R,B}/h_{R,0} \tag{30}$$

is the ratio between the edge-to-center density ratio corresponding to the high magnetic field transport solution (weak electric field approximation) $h_{R,B}$, and $h_{R,0}$. The coefficient $h_{R,B}$ is[19]

$$h_{R,B} = 1.25 \frac{v_{Te}}{R\omega_c^2} \left(\frac{m_i}{m_e}\right)^{1/2} \nu_e \tag{31}$$

where $v_{Te} = (k_B T_e/m_e)^{1/2}$ is the electron thermal velocity, and $\omega_c = eB/m_e$ is the electron cyclotron frequency. The $h_{R,0}$ coefficient is again provided in the book of Lieberman and Lichtenberg[13] an is

$$h_{R,0} = 0.8 \left(4 + \frac{R}{\lambda_i} + 0.41 \frac{T_i}{T_e} \frac{R^2}{\lambda_i^2}\right)^{-1/2} \tag{32}$$

Recent theoretical works[14, 17] have shown that the classical h coefficients in the magnetized case are only correct when no instability develops. The transition between the classical steady-state regime and the instability-enhanced transport regime was investigated in Cartesian coordinates. It was found that the transport can be correctly modeled using an effective collision frequency ν_{eff} in the directions perpendicular to the magnetic field lines. With the help of extensive 2D PIC simulations of an argon ICP, the following expression was found

$$\nu_{\text{eff}} = \nu_e \left[1 + 0.1 \left(\frac{h_{R,0}R}{\nu_e v_{Te}}\right)^2 \frac{m_e}{m_i} \omega_c^4\right]^{1/2} \tag{33}$$

This expression was originally found in Cartesian coordinates and is used here as is in cylindrical coordinates. These expressions were found within a certain set of assumptions that are summarized below.

- The plasma is isothermal;

- The electronegativity is limited;

- $m_i \nu_i \ll m_e \nu_e$ for all the ion species;

- The ions are weakly magnetized;

- Tha plasma is weakly ionized;

- The magnetic field points towards the thrust axis and its intensity is uniform.

The more detailed study was performed in argon and the results are here freely transfered to xenon. However, similar instabilities were observed in PIC simulations of a xenon ICP, as explained below.

An example of 2D PIC simulation of an xenon ICP discharge is provided as an illustration in Figure 2. In this simulation performed with the LPPic code, the grid is 400×400 and the time step is equal to 3.3×10^{-11} s. The LPPic code is an explicit electrostatic PIC Fortran code parallized using MPI. The reaction set for xenon is the same as in the xenon global model, and the implementation of the collision moodule has already been described elsewhere. The heating mechanism used for this simulation has already been described in several journal papers.[15, 16] In this simulation the discharge domain is 3×3 cm large and the gas pressure is set to 3 mTorr. The magnetic field is uniformly equal to 10 mT and is along the z direction, perpendicularly to the simulation plane. The instability pattern has a wavelength of about 1 mm and a frequency of about 3 MHz. The phase velocity of the instability is herfore of the order of magnitude of the Bohm speed. More details about the properties of this resistive drift wave instability can be found in former papers.[14] On a short time-scale, the plasma is not at steady-state, although time-averaged plasma properties can be defined on a time-scale larger than $10 \,\mu$s. The fast fluctuations have a strong influence on the global plasma transport. A first correction to take into account thee effects is to use a formula such as Eq. (33). In principle, the effective collision frequency ν_{eff} should vary across the discharge domain. However, the PIC simulation has shown that it remains reasonably constant in the quasineutral region of the plasma.
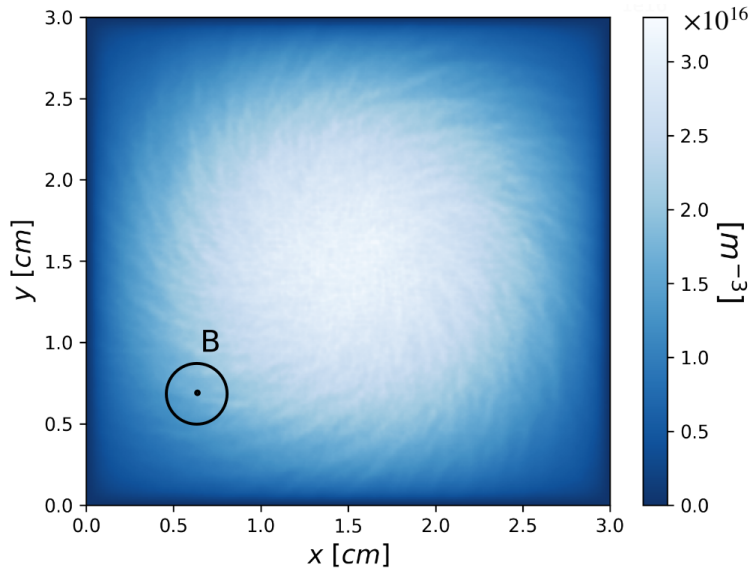
Figure 2. Map of the electron density in a 2D PIC simulation of a xenon inductive discharge at 3 mTorr of gas pressure and 9.6 kW/m^3 of absorbed power. The magnetic field is equal to 10 mT and is perpendicular to the simulation plane.

E.   Thruster parameters

The thruster parameters are inspired from the parameters of the Avant-Space experimental system described in Kralkina et al.[12] The useful parameters for the proposed global are provided in Table 3. Here, the radius of the thruster is the radius of the chamber itself. The radius of the heating coil or the electromagnet are not taken into account. The inlet gas flow is set to 4 sccm. The absorbed power is varied between 10 and 200 kW/m^3, while the magnetic field strength is varied between 0 and 20 mT. The geometrical grid transparency is equal to $\beta_g = 0.25$, which means that 25 % of the neutrals that hit the thruster inner surface defined by $z = L$ leave the discharge chamber. The outlet surface area for the neutrals is therefore

$$S_g = \beta_g \pi R^2 \tag{34}$$

Similarly, the ions leave the discharge through an effective surface area S_i which is larger than the geometrical surface S_g due to an electrostatic lens effect through the grids.

$$S_i = \beta_i \pi R^2 \tag{35}$$

From Alexandrov et al.,[1] $\beta_i = 0.6$. The power coupling efficiency ζ is here fixed to 60 %, which is in good agreement with previous detailed studies on the inductive power coupling in analog thruster configurations.[12]

Parameter	Description	Value	Unit
R	Radius	5	cm
L	Length	10	cm
β_g	Grid transparency	0.25	
β_i	Ion transparency	0.6	
Q	Gas flow rate	4.0	sccm
$\mathcal{P}_{RF}$	RF power	$10-40$	W
P_{abs}	Absorbed power	$7.6-30.6$	kW/m^3
ζ	Power coupling efficiency	0.6	
B	Magnetic field	$0-20$	mT

Table 3. Physical parameters used for the simulation of the xenon and iodine thrusters.

III. Results

The advantage of global models is that they can provide very fast estimates of the plasma characteristics and the thruster performances. Here, the main focus is on the effect of the magnetic field, so we provide a number of parametric studies with respect to the magnetic field produced by the electromagnet, between 0 and 20 mT. Two power regimes – 10 W and 40 W – are investigated that correspond to typical values of power for micro-satellite thrusters. Two models for the radial plasma transport are also studied. The first one is the instability-enhanced transport regime described above. The second model consists in using classical transport coefficients ($\nu_{\text{eff}} = \nu_e$) only.

A.   Plasma characteristics

XENON

The plasma characteristics predicted inside the xenon thruster are provided in Figure 3. First, as a consequence of the magnetic confinement, the electron density increases and the electron temperature decreases at higher magnetic field. Due to a more efficient ionization, the gas density also decreases when the confinement is better.

Second, we observe that the effects of the magnetic field saturates from approximately 10 mT onwards. This effect is visible both in the classical and the instability-enhanced model. In the classical model, the ion losses towards the side walls, characterized by the coefficient h_R which is proportional to B^{-2}, become very small. Therefore, at high magnetic fields, all the ions are lost in the $z = 0$ and $z = L$ end planes of the thruster. The magnetic field does not have any influence in the direction parallel to the field lines so the marginal effect of the magnetic field becomes negligible when the magnetic field is already so high that the radial losses are much smaller than the axial losses.

In the instability-enhanced regime, the axial losses remain the same but the h_R coefficient does not go to zero at high magnetic fields anymore. Instead, it saturates to a finite value that is approximately 30 % of the h_R factor without magnetic field. So the instability-enhanced transport regime predicts a weaker impact of the magnetic on the plasma properties.
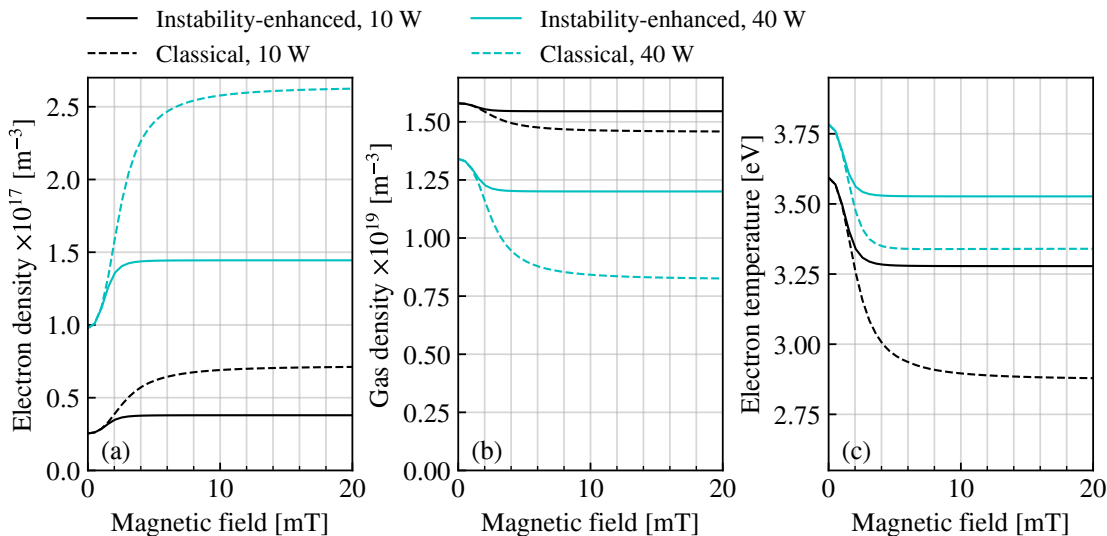

Figure 3.   Characteristics of the xenon plasma inside the thruster when varying the magnetic field from 0 to 20 mT at 10 W of RF power (black lines) and 40 W (cyan lines). The solid lines result from the full instability-enhanced model described above, and the dashed line the classical model ($\nu_{eff} = \nu_e$).

IODINE

The iodine model is more complex to interprete. The densities of the 6 species of the global model, as well as the electron temperature are presented a function of the magnetic field in Figure 4. The same regimes of power and the same models as previously are investigated.

It can be verified that the plasma electronegativity, defined as the ratio n_{I^-}/n_e, is significantly below one, such that the formulae for the h factors, that come from the theory of electropositive gases, should provide correct orders of magnitudes. For more details on the h factors in electronegative plasmas, the interested reader can refer to Chabert.[3] The effect of the plasma confinement are analogous to the xenon case: the electron density increases and the electron temperature decreases with the magnetic field. At high magnetic fields, the lower electron temperature could allow more negative ions to form through dissociative attachment. However, since the density of I_2 decreases with the magnetic field, both effects balance each other out and the density of negative ions is not very much influenced by the magnetic field. As a result, the plasma electronegativity decreases with the magnetic field.

At 40 W, I_2 depletion becomes dominant and the density of negative ions is reduced by about 30 when the magnetic field is varied from 0 to 20 mT. At lower power (10 W), the density of I increases with the magnetic field, possibly because I atom ionization becomes unlikely when the electron temperature becomes too low (the ionization energy of I is higher than the ionization and dissociative ionization energies of the I_2 molecule).

B.   Thruster efficiency

There are several variables of interest to study the performance of a thruster. Among them, the thrust, the thrust power efficiency, and the mass utilization efficiency are defined below and computed in the case of the xenon thruster and the iodine thruster.

The thrust is composed of one part due to the flux of ions accelerated through the grid, and one part coming from the thermal flux of neutrals.

$$T = h_L n_{Xe^+} S_i u_{B,Xe^+} m_{Xe} \left(\frac{eV_{grid}}{m_{Xe}} \right)^{1/2} + \frac{1}{4} n_{Xe} \overline{v}_{Xe}^2 m_{Xe} S_g \tag{36}$$

for xenon and

$$T = h_L S_i (eV_g rid)^{1/2} \left(n_{I^+} u_{B,I^+} m_I^{1/2} + n_{I_2^+} u_{B,I_2^+} m_{I_2}^{1/2} \right) + \frac{S_g}{4} \left(n_I \overline{v}_I^2 m_I + n_{I_2} \overline{v}_{I_2}^2 m_{I_2} \right) \tag{37}$$

for iodine.

The thrust power efficiency is estimated from the plume power. Again both the positive ion species and the neutral gas species need to be taken into account when computing the plume power.

$$\mathcal{P}_{plume} = h_L n_{Xe^+} S_i u_{B,Xe^+} eV_{grid} + \frac{1}{8} m_{Xe} n_{Xe} \overline{v}_{Xe}^3 S_g \tag{38}$$

for xenon and

$$\mathcal{P}_{plume} = h_L S_i eV_{grid} (n_{I^+} u_{B,I^+} + n_{I_2^+} u_{B,I_2^+}) + \frac{S_g}{8} (m_I n_I \overline{v}_I^3 + m_{I_2} n_{I_2} \overline{v}_{I_2}^3) \tag{39}$$

for iodine.

The thrust power efficiency is defined as

$$\gamma = \frac{\mathcal{P}_{plume}}{\mathcal{P}_{plume} + \mathcal{P}_{RF}} \tag{40}$$

where the RF power $\mathcal{P}_{RF}$ is linked to the power density absorbed by the plasma through

$$P_{abs} V = \zeta \mathcal{P}_{RF} . \tag{41}$$

ζ is the power coupling efficiency, set to 0.6 throughout this paper. Finally, the mass utilization efficiency is the ratio between the mass flow of the accelerated and the inlet mass flow rate of the gas:

$$\eta = \frac{h_L n_{Xe^+} S_i u_{B,Xe^+}}{Q} \tag{42}$$

for xenon, and

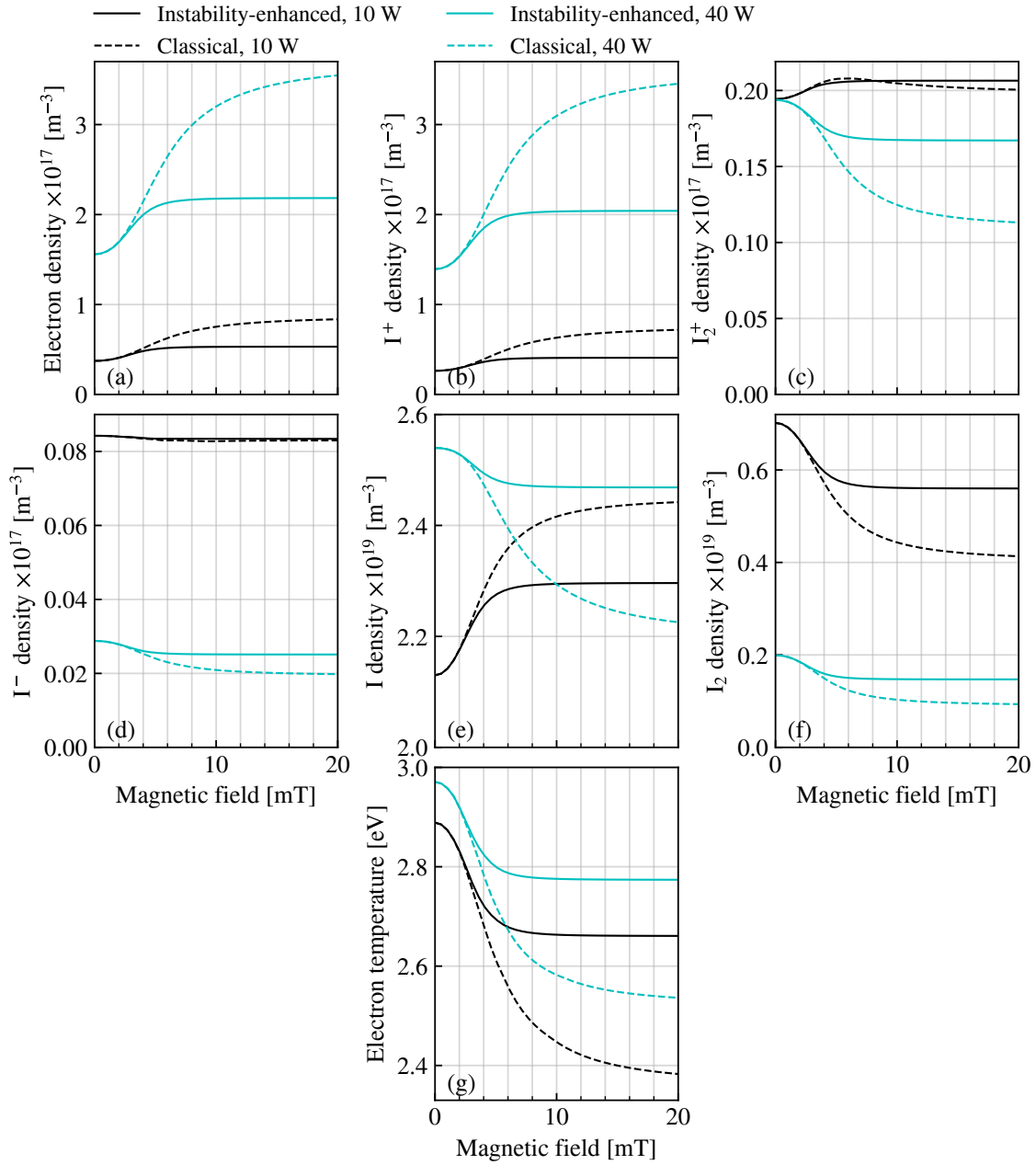$$\eta = \frac{h_L S_i (n_{I^+} u_{B,I^+} m_I + n_{I_2^+} u_{B,I_2^+} m_{I_2})}{m_{I_2} Q} \tag{43}$$

Figure 4. **Characteristics of the plasma inside the iodine thruster when varying the magnetic field from 0 to 20 mT at 10 W of RF power (black lines) and 40 W (cyan lines). The solid lines result from the full instability-enhanced model described above, and the dashed line the classical model ($\nu_{eff} = \nu_e$).**

for iodine. The results obtained for the three variables T, γ, and η are presented in Figures 6 and **??** as a function of the magnetic field.

In the range of power investigated here, the thrust power efficiency does not seem very much affected by the value of the power. The thrust, however, seems almost proportional to the RF power, which seems reasonable since the plasma is weakly ionized. The thrust predicted by the classical model at high magnetic fields is 55 % higher than the value predicted by the istability-enhanced transport model at 40 W of RF power. In general, the classical model seems to systematically overestimate the performances of the thruster.

The performances of the iodine thruster are quite similar to the xenon thruster and terms of thrust and thrust power efficiency. According to the model, the thrust is even significantly higher when iodine is used. However, the mass utilization efficiency of the iodine thruster is poorer than the xenon thruster.
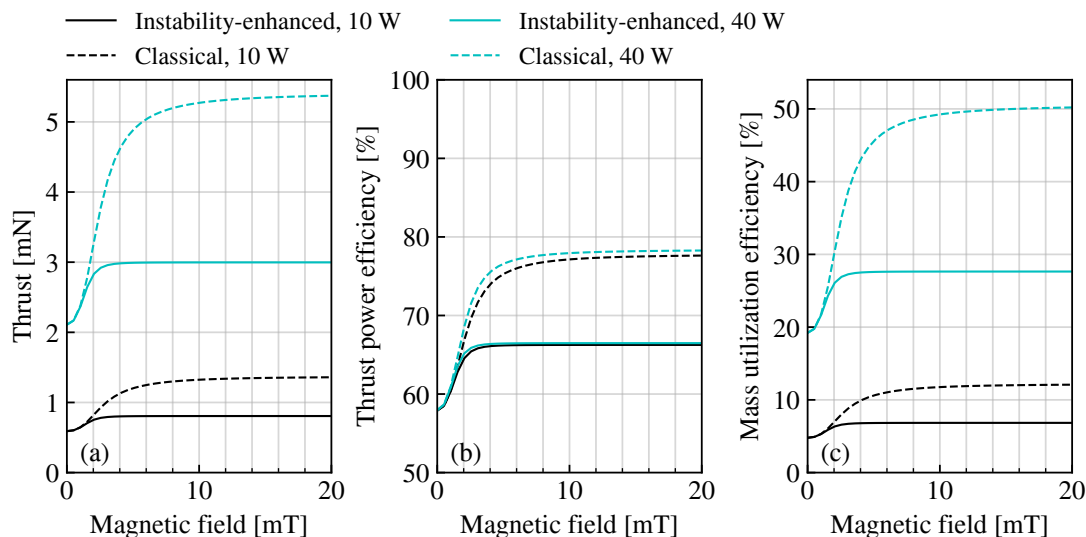

Figure 5. Xenon thruster performances when varying the magnetic field from 0 to 20 mT at 10 W of RF power (black lines) and 40 W (cyan lines). The solid lines result from the full instability-enhanced model described above, and the dashed line the classical model ($\nu_{eff} = \nu_e$).
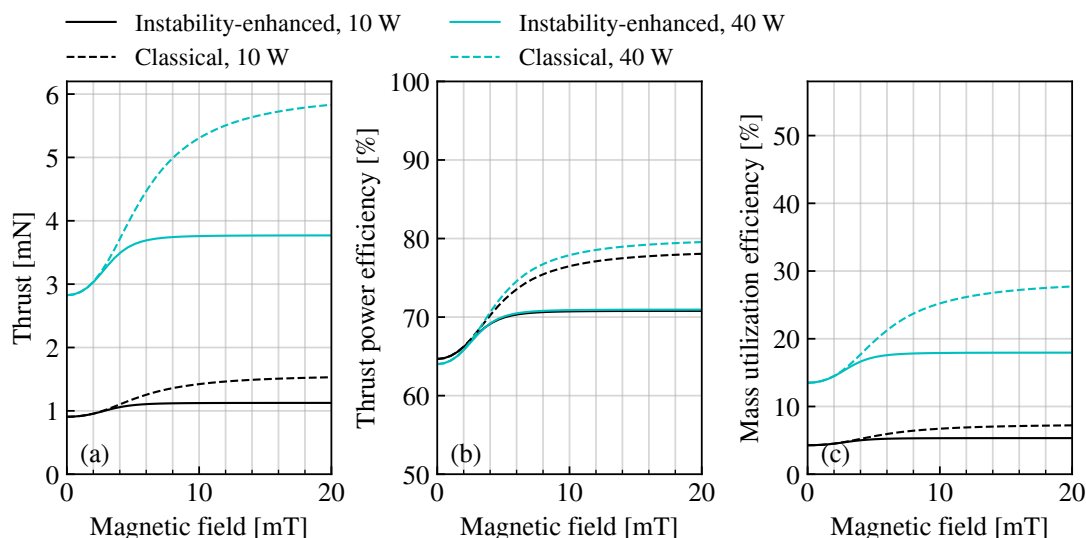

Figure 6. Iodine thruster performances when varying the magnetic field from 0 to 20 mT at 10 W of RF power (black lines) and 40 W (cyan lines). The solid lines result from the full instability-enhanced model described above, and the dashed line the classical model ($\nu_{eff} = \nu_e$).

IV.   Conclusion

Adding an axial magnetic field in a GIT improves the electron confinement and yields better overall performances. This effect is accounted for in a global model by introducing modified edge-to-center plasma density ratios (h factors) in the cross field (radial) direction. The new global model is able to quantify the benefit of adding an electromagnet to thruster design. However, classical theories overestimate magnetic confinement. At high magnetic fields, h factors depend on the electron dynamics which is very much affected by resistive drift instabilities, as it has been shown by a PIC simulation of a xenon discharge. An effective electron collision frequency is used here to account for the radial electron transport inside the discharge chamber. This more realistic transport model reduces the theoretical benefit of adding a magnetic field. Multiple global model simulations of a typical small GIT operated with xenon and iodine were performed. When using iodine, the electronegativity decreases with the magnetic field. Within the parameter range investigated here, iodine and xenon thrusters yield similar performances in terms of thrust and thrust power efficiency. However, the iodine thruster has a much lower mass utilization efficiency.

The models are valid under a number of assumptions that need to be verified experimentally or using more sophisticated simulation tools. In particular, the h factor, and the instability-enhanced transport coefficients are valid for weakly ionized, low electronegativity, isothermal plasmas.

For real thruster design, the choice of adding a magnetic circuit results from a trade-off between cost, mass and volume occupancy on the one hand, and performance optimization on the other hand. Global models can be handy tools to make this trade-off in early design phase. However, the fact that power coupling efficiency was fixed in this paper, limits that model predictability. Finally, comparison with experimental data would be very useful to validate the model.

Acknowledgments

References

[1] ALEXANDROV, A. F., KRALKINA, E. A., PAVLOV, V. B., AND RUKHADZE, A. A. On the Possibilities of RF Ion Thruster Optimization. In *29th Electric Propulsion Conference* (Princeton University, 2005), vol. IEPC-2005-122, p. 18.

[2] BIAGI, S. F. Programm magboltz v7.1. cross section compilation. see www.lxcat.net. retrieved on November 16, 2016, 2004.

[3] CHABERT, P. An expression for the h_l factor in low-pressure electronegative plasma discharges. *Plasma Sources Science and Technology 25*, 2 (2016), 025010.

[4] CHABERT, P., ARANCIBIA MONREAL, J., BREDIN, J., POPELIER, L., AND AANESLAND, A. Global model of a gridded-ion thruster powered by a radiofrequency inductive coil. *Physics of Plasmas 19*, 7 (2012), 073512.

[5] CHABERT, P., AND BRAITHWAITE, N. *Physics of Radio-Frequency Plasmas*. Cambridge University Press, 2011.

[6] DESPIAU-PUJO, E., AND CHABERT, P. Global model of instabilities in low-pressure inductive chlorine discharges. *Plasma Sources Science and Technology 18*, 4 (2009), 045028.

[7] GREAVES, C. Ion-Ion Recombination in Iodine Afterglows. *Journal of Electronics and Control 17*, 2 (1964), 171–180.

[8] GRONDEIN, P., LAFLEUR, T., CHABERT, P., AND AANESLAND, A. Global model of an iodine gridded plasma thruster. *Physics of Plasmas 23*, 3 (2016), 033514.

[9] HAMILTON, J. R. Iodine: I_2 molecule and I atom. Tech. rep., Quantemol Ltd, 2015.

[10] HAMILTON, J. R. Consultancy project for LPP. I_2 and I^- data. Tech. rep., Quantemol Ltd, 2017.

[11] HUANG, S., AND GUDMUNDSSON, J. T. A particle-in-cell/Monte Carlo simulation of a capacitively coupled chlorine discharge. *Plasma Sources Science and Technology 22*, 5 (2013), 055020.

[12] KRALKINA, E., ZADIRIEV, I., AND KHARLAN, A. Exploratory Testing of a Radio-Frequency Thruster for Small Satellites. In *35th Electric Propulsion Conference* (Atlanta, 2017), vol. IEPC-2017-425.

[13] LIEBERMAN, M. A., AND LICHTENBERG, A. J. *Principles of plasma discharges and materials processing*, 2nd ed. Wiley-Interscience, 2005.

[14] LUCKEN, R., BOURDON, A., LIEBERMAN, M. A., AND CHABERT, P. Instability-enhanced transport in low temperature magnetized plasma. *Physics of Plasmas 26*, 7 (2019), 070702.

[15] LUCKEN, R., CROES, V., LAFLEUR, T., RAIMBAULT, J.-L., BOURDON, A., AND CHABERT, P. Global models of plasma thrusters: Insights from PIC simulation and fluid theory. In *IEPC* (2017), vol. 2017-323.

[16] LUCKEN, R., CROES, V., LAFLEUR, T., RAIMBAULT, J.-L., BOURDON, A., AND CHABERT, P. Edge-to-center plasma density ratios in two-dimensional plasma discharges. *Plasma Sources Science and Technology 27*, 3 (2018), 035004.

[17]LUCKEN, R., TAVANT, A., BOURDON, A., LIEBERMAN, M. A., AND CHABERT, P. Saturation of the magnetic confinement in weakly ionized plasma. *Accepted in Plasma Sources Science and Technology* (2019).

[18]SAKABE, S., AND IZAWA, Y. Simple formula for the cross sections of resonant charge transfer between atoms and their positive ions at low impact velocity. *Physical Review A 45*, 3 (1992), 2086.

[19]STERNBERG, N., GODYAK, V., AND HOFFMAN, D. Magnetic field effects on gas discharge plasmas. *Physics of Plasmas 13*, 6 (2006), 063511.

[20]TENNYSON, J., BROWN, D. B., MUNRO, J. J., ROZUM, I., VARAMBHIA, H. N., AND VINCI, N. Quantemol-N: an expert system for performing electron molecule collision calculations using the R-matrix method. *Journal of Physics: Conference Series 86* (2007), 012001.

[21]YEUNG, T. H. Y. Recombination coefficients for positive and negative ions. *Proceedings of the Physical Society 71*, 3 (1958), 341.